Improved Visible Light-Driven Catalytic Activity in Type-Ⅰ Heterojunction of CZTS/g-C_3N_4

LI Yufang[1*], *HOU Zhangchen*, *LIU Jinsong*, *SHI Zheng*, *SHEN Honglie*

College of Materials Science and Technology, Jiangsu Key Laboratory of Materials and Technology for Energy Conversion, Nanjing University of Aeronautics and Astronautics, Nanjing 211106, P. R. China

(Received 7 March 2022; revised 14 July 2022; accepted 30 December 2022)

Abstract: In order to increase the rate of Cu_2ZnSnS_4 (CZTS) photocatalytic degradation of Rhodamine B (RhB), type-Ⅰ heterojunction of the CZTS/g-C_3N_4 composite structure was successfully prepared by a hydrothermal method in this work. CZTS/g-C_3N_4 is applied in photocatalytic degradation of the colored dye RhB. The results showed that g-C_3N_4 was attached to the surface of flower-like CZTS, and the two formed a type-Ⅰ heterojunction. CZTS acted as an electron trap for g-C_3N_4, which improved the separation efficiency of carriers. The results of photocatalytic degradation of RhB showed that CZTS/g-C_3N_4 composite structure could improve the photocatalytic degradation effect of RhB. The best photocatalytic efficiency of RhB was 98.63% within 60 min.

Key words: photocatalysis; hydrothermal; CZTS/g-C_3N_4; photogenerated carriers; heterojunction

CLC number: TN925 **Document code:** A **Article ID:** 1005-1120(2023)03-0293-14

0 Introduction

Organic wastewater and harmful waste gas produced in industrial production make environmental pollution increasingly serious. Environmental pollution has posed a significant threat to the progress of human society and economic development, and solving environmental pollution has become an important issue for society[1-2].

As a new green environmental protection technology, photocatalytic technology is an excellent alternative for environmental pollution control and new energy development. Photocatalytic technology uses semiconductor materials as a medium to absorb solar energy and then converts it into chemical energy, which can promote the decomposition of organic pollutants and achieve the purpose of protecting the environment[3-4]. Due to their strong physical and chemical properties, metal oxide semiconductor materials have been used in the field of photocatalysis for a long time[5-6]. Among them, TiO_2[7-9] has attracted attention due to its easy preparation, good economic benefits, and stable properties. In addition, some sulfide semiconductor materials[10-12] also have good photocatalytic properties. However, due to the wide bandgap of these photocatalytic materials, the utilization rate of sunlight is too low, which affects their application in the field of photocatalysis. To improve the utilization rate of sunlight, it is necessary to find a kind of semiconductor photocatalyst with a narrow bandgap and economic and environmental benefits.

The multicomponent compounds have a small bandgap that can absorb sunlight, especially visible light. CZTS is a direct bandgap semiconductor with a bandgap of about 1.5 eV[13]. It can absorb visible light and even near-infrared light[14], so it is first widely used in the field of solar cells[15]. Besides, the chemical properties of CZTS are stable[16], and the four components of CZTS are abundant in nature, which will not harm the environment[17]. In addition, the preparation methods of CZTS are diver-

*Corresponding author, E-mail address: lyf_msc@nuaa.edu.cn.

How to cite this article: LI Yufang, HOU Zhangchen, LIU Jinsong, et al. Improved visible light-driven catalytic activity in type-Ⅰ heterojunction of CZTS/g-C_3N_4[J]. Transactions of Nanjing University of Aeronautics and Astronautics, 2023, 40(3): 293-306.

http://dx.doi.org/10.16356/j.1005-1120.2023.03.006

sified and relatively simple[18-19]. The prepared CZTS can be used for photocatalytic degradation of harmful gases, antibiotics, organic dyes and other pollutants, sterilization and disinfection, and hydrogen production from water[20-21]. In recent years, CZTS has made some advances in the application of photocatalysis. However, CZTS has the drawbacks of easy recombination of photogenerated carriers and low degradation efficiency.

An efficient approach to minimize carrier recombination is to combine CZTS with other semiconductors. At present, the semiconductors forming composite structures with CZTS mainly include metal oxide semiconductors (TiO_2[22], SnO_2[23], ZnO[24], WO_3[25], CeO_2[26], Bi_2WO_6[27], $ZnFe_2O_4$[28]) and a small amount of sulfide semiconductors (CdS[29], MoS_2[30]). Due to the unique electronic structure of each semiconductor, the composite heterostructures formed by CZTS and different semiconductors are also different, and the photocatalytic effect is also different.

g-C_3N_4 is a type of semiconductor polymer material that has been widely studied in recent years due to its graphite-like layered structure, unique molecular structure, good stability and conductivity[31-33]. In recent years, g-C_3N_4 has also been widely used in the field of photocatalysis. However, as a photocatalyst, g-C_3N_4 has the disadvantages of large forbidden band width and easy recombination of photogenerated carriers. Among them, compounding g-C_3N_4 with other compounds is an effective method to improve the photocatalytic efficiency of g-C_3N_4. Experiments have demonstrated that both Ag_3PO_4/P-g-C_3N_4[34] and Ag_2S/K-g-C_3N_4[35] synthesis can increase the BET surface area, broaden the visible light response region, and have high photocatalytic hydrogen production efficiency. In addition, composites such as $AgNbO_3$/g-C_3N_4[36] and $KTa_{0.75}Nb_{0.25}O_3$ (KTN)/g-C_3N_4[37] display longer lifetimes of photoexcited carriers, elevating the photocatalytic dehydrogenation performance of g-C_3N_4.

From the energy band structure point of view, the highest electron occupied molecular orbital (HOMO) and lowest electron unoccupied molecular orbital (LUMO) of g-C_3N_4 are lower and higher than the valence band and conduction band of CZTS, respectively. Therefore, the combination of the two forms a type-Ⅰ heterojunction. Although the type-Ⅰ heterojunction has no substantial effect on the separation of photogenerated carriers, the yield of photogenerated carriers can be increased and the photocatalytic effect can be enhanced. The application of CZTS complexes with g-C_3N_4 for photocatalysis has been reported. The results showed that CZTS/g-C_3N_4 has a good photocatalytic degradation effect on trichloroethylene[38]. However, the application of CZTS/g-C_3N_4 to photocatalytic organic dyes has not been reported yet. The textile printing and dyeing industry has a large amount of sewage discharge, and the sewage often contains a large number of complex and chemically stable macromolecular organic pollutants, including various dyes, additives, dyeing auxiliaries and other chemically harmful substances. At present, the types of dyes used in printing and dyeing have reached tens of thousands, and many of them have carcinogenic hazards. RhB is one of the dyes that can cause cancer. This poses a serious threat to human health. By photocatalytic technology, organic dyes can be degraded into CO_2 and H_2O, which can reduce the harm to the environment and human body.

In this work, flower-like CZTS and flake g-C_3N_4 were combined to form the composite structure of CZTS/g-C_3N_4 by a simple hydrothermal method, which sped up the photocatalytic rate. As visible light was used as the light source, the photocatalytic degradation effect of CZTS/g-C_3N_4 composite structure on RhB in solution was studied. The photocatalytic activity free radical capture experiment was carried out, and the process of photocatalytic degradation of RhB with the CZTS/g-C_3N_4 composite structure was explored.

1 Material and Methods

All chemicals and solvents used in the experiment were produced by Nanjing Chemical Reagent Co., Ltd. (China). And they could all be used directly.

1.1 Preparation of flower-like CZTS nanomaterials

The flower-like CZTS nanomaterials were synthesized by a hydrothermal method. 2 mM $Cu(NO_3)_2 \cdot 3H_2O$, 1 mM $Zn(CH_3COO)_2 \cdot 2H_2O$, 1 mM $SnCl_2 \cdot 3H_2O$ and 4 mM thiourea were successively added into a beaker containing distilled water. After the solution was uniformly stirred, the solution was loaded into a hydrothermal reactor. Placed the reaction kettle in a drying oven for heat preservation treatment. The temperature was set to 200 ℃ and the holding time was 24 h. After the reaction, the reactants were taken out, cleaned and dried to obtain CZTS nanomaterials.

1.2 Preparation of flake g-C_3N_4

First, bulk g-C_3N_4 was prepared by a sintering method. 10 g of melamine was placed in a crucible, wrapped with aluminum foil and place in the muffle furnace. After the temperature rose to 550 ℃, the material was kept for 3 h to obtain the yellow bulk g-C_3N_4. Second, g-C_3N_4 was stripped of concentrated sulfuric acid. The bulk g-C_3N_4 was added and the above was perpared into concentrated sulfuric acid and stired evenly. It was then slowly poured into 500 mL of distilled water. The yellow g-C_3N_4 became white and was placed for 1 h. The white g-C_3N_4 mixed solution was taken out and placed in the centrifuge tube, and centrifuged at 2 500 r/min for 5 min. The upper suspension was detached, then centrifuged and washed to neutral at 9 000 r/min. The white flake g-C_3N_4 was produced after drying.

1.3 Preparation of CZTS/g-C_3N_4 composite structure

The CZTS/g-C_3N_4 was synthesis prepared by the hydrothermal method. A certain amount of flake g-C_3N_4 and CZTS were added to 25 mL H_2O, stirred for 30 min, and then put into the reactor. The temperature was set to 200 ℃. After 24 h of incubation, the samples were taken out and centrifuged to obtain the CZTS/g-C_3N_4 samples. The mass fractions of g-C_3N_4 in the CZTS/g-C_3N_4 samples were 5%, 10% and 15%, which were denoted as CZTS/g-C_3N_4-1, CZTS/g-C_3N_4-2 and CZTS/g-C_3N_4-3, respectively.

1.4 Measurements and characterization

The microscopic morphology of the sample was observed by Hitachi S-4800 scanning electron microscope (SEM), and its element composition was analyzed by X-ray energy spectrometer (EDS). BrukerD8-Discover X-ray diffractometer was used to analyze the crystal structure and phase composition of the samples (XRD). The valence state of elements in the sample was analyzed by Escalab 250 Xi X-ray photoelectron spectrometer (XPS).

1.5 Photoelectrochemical measurements

The electrochemical workstation of a three-electrode system was used to characterize the photoelectric chemical properties of the samples. The working electrode was prepared by evenly coating the sample onto the conductive glass by a spin coating method, and then heated at 70 ℃. All measured potential values in the experiment were relative saturated calomel reference electrode potential (relative to SCE). The Pt electrode was used as the auxiliary electrode. The main contents of the test included photocurrent test, AC impedance test and linear sweep voltammetry test. The electrolyte was a mixed solution of Na_2S and NaOH when the photocurrent was tested. The working electrode was intermittently exposed to light. When the AC impedance was tested, the test was performed in a dark state, and the electrolyte was Na_2SO_4 solution.

1.6 Photocatalytic degradation measurements

In the photocatalytic process, the light source was a xenon lamp (150 W, $\lambda > 420$ nm), and the prepared CZTS, g-C_3N_4 and CZTS/g-C_3N_4 samples were used as photocatalysts for photocatalytic degradation of RhB. 10 mg·L^{-1} RhB solution was used as degradation substrate, and a 100 mL solution was taken for each experiment. Then 30 mg CZTS, g-C_3N_4 and CZTS/g-C_3N_4 samples were added. Before the illumination process, the sample was darkened to achieve the adsorption-desorption equilibrium of RhB. After starting the illumination, a 6 ml solution was taken into the centrifuge tube every 10 min, and the illumination was

stopped after some time. Finally, after the solution was centrifuged, the concentration change of the supernatant was analyzed by a UV-vis spectrophotometer.

The relationship between the concentration of RhB solution and its absorbance could be obtained by the Lambert-Beer law as

$$A=\lg(I_0/I)=\lg(1/T)=kcb \quad (1)$$

where A is the absorbance; the ratio of output light intensity I to incident light intensity I_0 is defined as the transmittance T of the solution to be tested; k is the molar absorption coefficient; c the concentration of the substance to be measured; and b the thickness of the absorption layer. According to Eq.(1), the concentration of the solution could be obtained, and according to the Eq.(2), the degradation efficiency of RhB could be obtained in a certain time D, shown as

$$D=(c_0-c_t)/c_0\times 100\% \quad (2)$$

where c_0 is the original concentration of the solution before illumination and c_t the solution concentration of RhB at time t after turning on the xenon lamp.

2 Results and Discussion

2.1 SEM analyses

The SEM images of g-C_3N_4 before and after peeling and dispersion, CZTS and CZTS/g-C_3N_4 composite structures were shown in Fig.1. Figs.1(a,b) show the microscopic morphology of bulk g-C_3N_4 and flake g-C_3N_4, respectively. It could been seen that after the exothermic stripping with concentrated sulfuric acid, the microscopic morphology of g-C_3N_4 changed from a large block structure to a small flaky structure. Fig.1(c) shows the microscopic morphology of CZTS prepared at 200 ℃ with H_2O as a solvent. Figs.1(d—f) show the composite structure samples of CZTS/g-C_3N_4-1, CZTS/g-C_3N_4-2 and CZTS/g-C_3N_4-3, respectively. The morphology of the composite structure samples showed the form of sheet-like g-C_3N_4 wrapped CZTS. The size of the composite structure samples was similar to that of CZTS. However, after further hydrothermal holding at 200 ℃ for 24 h, the thickness of CZTS nanosheets increased, and as

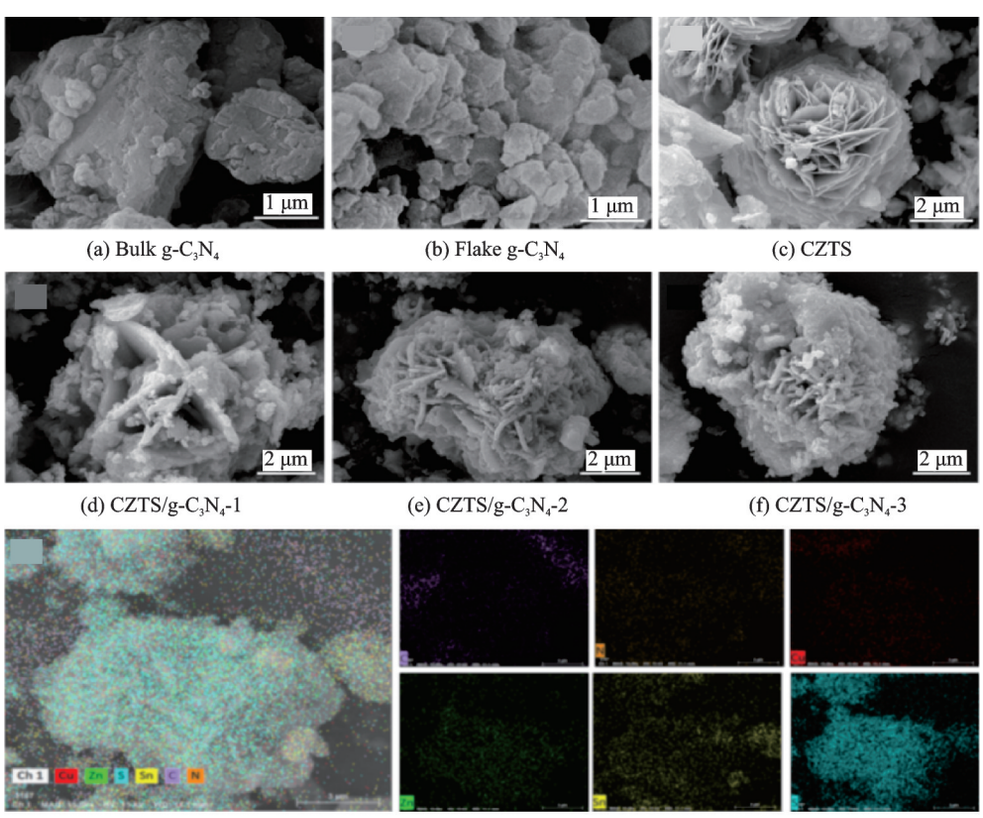

Fig.1 SEM images and EDS of g-C_3N_4 before and after peeling and dispersion, CZTS and CZTS/g-C_3N_4

the content of g-C_3N_4 in the CZTS/g-C_3N_4 composite structure increased, more and more g-C_3N_4 were wrapped around CZTS. The EDS of the CZTS/g-C_3N_4-2 sample was shown in Fig.1(g). It could be seen that the prepared CZTS/g-C_3N_4 samples contained Cu, Zn, Sn, S, N, C elements, indicating that the CZTS/g-C_3N_4 was successfully prepared.

2.2 XRD analysis

Fig.2 shows the phase structure of g-C_3N_4, CZTS and CZTS/g-C_3N_4 samples characterized by XRD. The main diffraction peaks of bulk g-C_3N_4 were matched with the standard card of g-C_3N_4 (JCPDS 87-1526)[39]. In the spectrum, the characteristic diffraction peak of the (100) crystal plane corresponded to the 12.90° diffraction peak, and the characteristic diffraction peak of the (002) crystal plane corresponded to the 27.34° diffraction peak. There were no other impurity diffraction peaks in the diffraction pattern, which indicated that the sample was pure g-C_3N_4. The flake g-C_3N_4 showed (002) crystal plane was at 27.34°, while (100) crystal plane at 12.90° almost disappeared. The (002) crystal plane of g-C_3N_4 at 27.3° corresponded to the interlayer structure of g-C_3N_4[40]. The (100) crystal plane of g-C_3N_4 at 12.90° was mainly caused by the orderly arrangement of internal condensed melamine units[41-42]. Compared to bulk g-C_3N_4, the diffraction peak at the (002) crystal plane of flake g-C_3N_4 was weakened, and the crystallinity decreased, but the position of the peak did not change, mainly due to the decrease of the stacking degree of g-C_3N_4 interlayer after exfoliation. Besides, the diffraction peak at the (100) crystal plane almost disappeared, leaving only one diffraction peak at the (002) crystal plane, indicating that the obtained sample was indeed flake g-C_3N_4[43]. The prepared CZTS sample was the kesterite structure CZTS (JCPDS 26-0575)[44]. The diffraction peaks of CZTS/g-C_3N_4 composite structure samples point to flake g-C3N4 and the kesterite structure CZTS, confirming the successful preparation of CZTS/g-C_3N_4 composite materials. As the content of g-C_3N_4 in the CZTS/g-C_3N_4 samples increased, the diffraction peak intensity of CZTS in the composite sample decreased, indicating that different g-C_3N_4 content would affect the diffraction peak intensity of CZTS/g-C_3N_4.

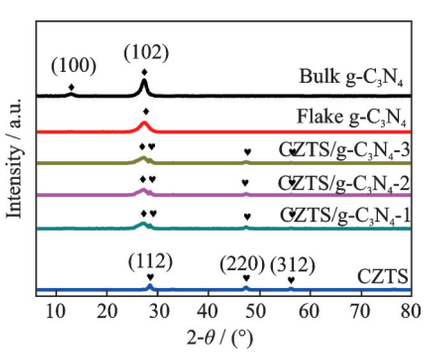

Fig.2 XRD patterns of g-C_3N_4, CZTS and CZTS/g-C_3N_4

2.3 XPS analysis

The composite structure of CZTS, g-C_3N_4, and CZTS/g-C_3N_4-2 were chemically analyzed by X-ray photoelectron spectroscopy (XPS) test. The results were shown in Fig.3. The binding energies of Cu 2p, Zn 3d, and Sn 3d of CZTS/g-C_3N_4-2 were slightly reduced compared with those of pure CZTS, indicating an increase in electron density. Compared with CZTS, there was almost no difference in the S 2p binding energy of CZTS/g-C_3N_4-2. The chemical valence state of CZTS/g-C_3N_4-2 was analyzed. It could be seen from the XPS high-resolution spectrum in Fig.3 that the CZTS/g-C_3N_4-2 composite structure contained six elements: Cu, Zn, Sn, S, C and N. The two characteristic peaks of Cu 2p appeared at 951.2 eV and 931.5 eV, corresponding to Cu $2p^{1/2}$ and Cu $2p^{3/2}$, respectively. The peak spacing of Cu $2p^{1/2}$ and Cu $2p^{3/2}$ was 19.7 eV, so the chemist valence state of Cu was +1. Fig.3(c) showed the two characteristic peaks of Zn 2p. The characteristic peaks appearing at 1 044.8 eV and 1 021.6 eV corresponded to Zn $2p^{1/2}$ and Zn $2p^{3/2}$, respectively. The peak spacing of Zn $2p^{1/2}$ and Zn $2p^{3/2}$ was 23.2 eV, which indicated the existence of Zn^{2+}. The two characteristic peaks of Sn 3d were shown in Fig.3(d). The characteristic peaks at 495.6 eV and 487.3 eV corresponded to Sn $3d^{3/2}$ and Sn $3d^{5/2}$, respectively, and the peak spacing between the two was 8.3 eV,

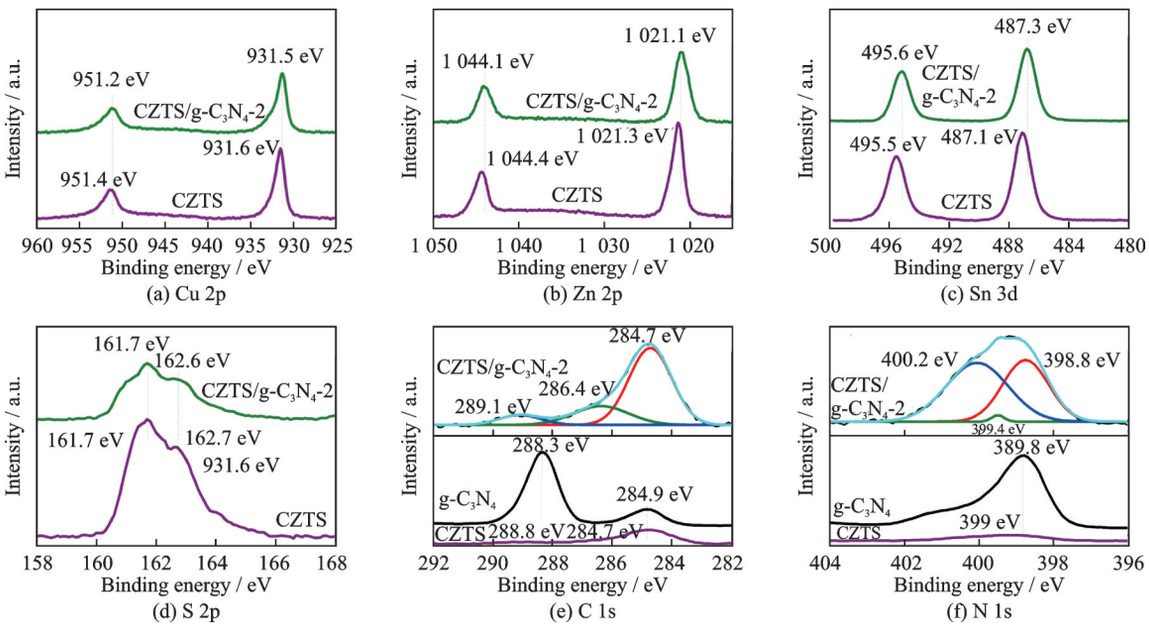

Fig.3 High resolution XPS results of the CZTS, g-C_3N_4 and CZTS/g-C_3N_4-2

which indicated that the chemical valence of Sn was +4. Fig.3(e) showed that the characteristic peaks of the S 2p spectrum corresponded to S $2p^{1/2}$ and S $2p^{3/2}$ at 162.6 eV and 161.7 eV, indicating that the S element existed in a chemical valence state of −2[45]. Fig.3(f) shows the peak separation of C 1 s, where the peak at 284.7 eV corresponded to sp^2 hybridization of C-C bond, the peak at 286.4 eV corresponded to sp^3 hybridization of C-NH_2 bond, and the peak at 288.5 eV corresponded to sp^2 hybridization of N-C=N bond[46]. Fig.3(g) showed the peak separation results of the N1s peak. The peak at 398.8 eV corresponded to the sp^2 hybridization of the C-N=C bond, the peak at 399.4 eV corresponded to the sp^3 hybridization of N (N-$[C]_3$) bond, and the peak at 200.2 eV corresponded to the N-NH_x bond of an amino-functional group[47].

2.4 DRS analysis

The UV-V is diffuse reflectance (DRS) test was performed on CZTS/g-C_3N_4 samples to study the optical characteristics of CZTS/g-C_3N_4. Fig.4 shows the DRS spectra and $(\alpha h\nu)^2$-$h\nu$ curves of CZTS, g-C_3N_4 and CZTS/g-C_3N_4. Fig.4(a) shows that the absorption edge of g-C_3N_4 was approximately between 400 nm and 450 nm. The light absorption edge of the CZTS/g-C_3N_4 composite structure samples were red-shifted relative to g-C_3N_4, which showed that the visible light absorption capacity has been enhanced. The band gaps of CZTS, g-C_3N_4 and CZTS/g-C_3N_4 were calculated by the Kubelka-Munk equation[48]. The optical band gap of g-C_3N_4 was 2.7 eV, and that of CZTS was 1.5 eV by extrapolation of the linear part in Fig.4(b) to the intersection with the abscissa. The bandgap of CZTS/g-C_3N_4 composite structures was 2.15 eV, 2.23 eV and 2.37 eV, which were between the bandgap of CZTS (1.5 eV) and g-C_3N_4 (2.7 eV). The calculated positions of LUMO and HOMO of g-C_3N_4 were −1.21 eV and 1.49 eV, respectively. The conduction band of CZTS was −0.45 eV, and the valence band was 1.05 eV. In combination with the g-C_3N_4 and CZTS band positions, the heterojunction type-Ⅰ was formed.

2.5 Photoelectrochemical analysis

As we all know, the photocatalytic effect of a semiconductor is related to its ability to separate photogenerated electrons and holes. The radius of the impedance arc in the Nyquist diagram reflects the impedance of the system, and indicates the difficulty of charge transfer at the system interface[49]. In order to analyze the separation and transport ability of photogenerated carriers of CZTS, g-C_3N_4 and CZTS/g-C_3N_4 samples, electrochemical tests were

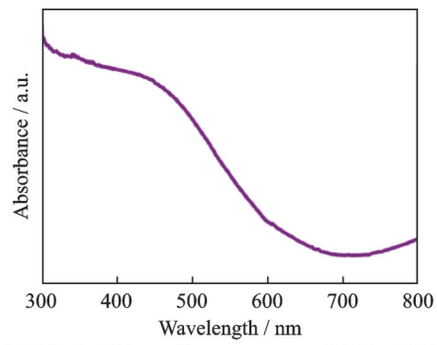

(a) UV-vis diffuse reflectance spectra (DRS) of CZTS

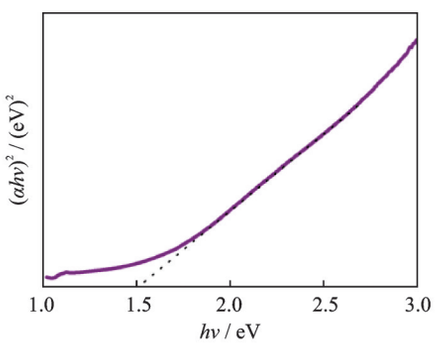

(b) Tauc's plot showing the estimation of band gap of CZTS

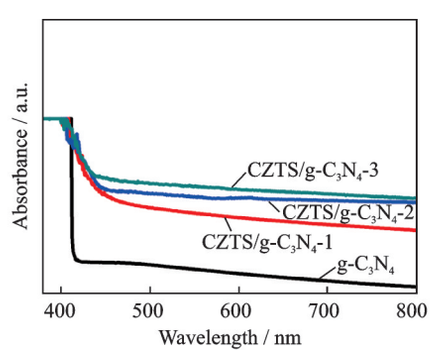

(c) UV-vis diffuse reflectance spectra (DRS) of g-C_3N_4 and CZTS/g-C_3N_4

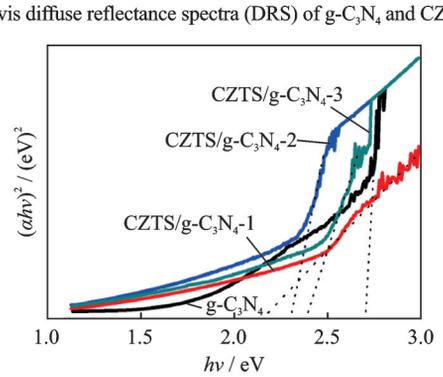

(d) Tauc's plot showing the estimation of band gap of g-C_3N_4 and CZTS/g-C_3N_4

Fig.4 UV-vis diffuse reflectance spectra (DRS) and Tauc's plot showing the estimation of band gap of CZTS, g-C_3N_4, and CZTS/g-C_3N_4

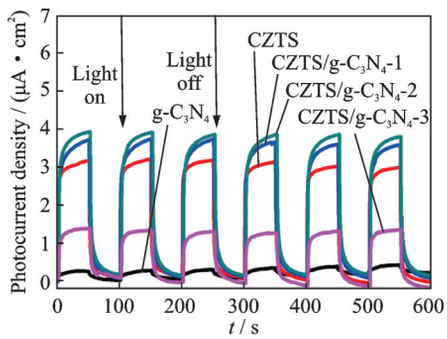

(a) Photocurrent density vs time curves

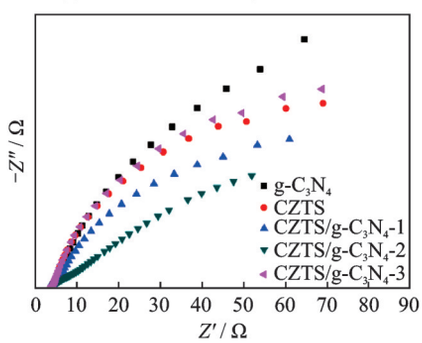

(b) Nyquist plots of measured EIS spectra of g-C_3N_4

Fig.5 Photocurrent density and nyquist plots of measured EIS spectra of g-C_3N_4

carried out on different samples. Fig.5(a) reveals the i-t curves of g-C_3N_4, CZTS and CZTS/g-C_3N_4 composite structures. After g-C_3N_4 and CZTS were composed, the maximum photocurrent density of CZTS/g-C_3N_4-1 and CZTS/g-C_3N_4-2 increased significantly. The maximum photocurrent densities of CZTS/g-C_3N_4 with different ratios were different, and the highest photocurrent density was CZTS/g-C_3N_4-2, which indicated that the ratio could effectively improve the quantum yield. For the CZTS/g-C_3N_4-3 composite structure, although the maximum photocurrent density was significantly higher than the maximum photocurrent density of g-C_3N_4, it was lower than that of CZTS. It may be that too much g-C_3N_4 was attached to the outside of CZTS which affected the optical absorption capacity of CZTS, and further affected the carrier generation and transfer process of the CZTS/g-C_3N_4-3. Fig.5(b) shows the electrochemical impedance spectroscopy (EIS) resulted from CZTS/g-C_3N_4 composite structures. The radius of the Nyquist diagram of the CZTS/g-C_3N_4-2 composite structure was the smallest, indicating that the driving force of its interface was the largest.

2.6 Photocatalytic degradation analysis

Under visible light irradiation, the photocatalytic degradation performance of g-C_3N_4, CZTS and CZTS/g-C_3N_4 composite structures on RhB was studied (Fig.6). As seen in Fig.6, the adsorption

capacity of g-C_3N_4 for RhB was very limited in the dark treatment. When g-C_3N_4 was combined with CZTS, the adsorption capacity of samples for RhB increased, indicating that CZTS played a role in the composite structures. However, with the increase of g-C_3N_4, the adsorption capacity decreased slightly, which may be attributed to the increase of g-C_3N_4 attached to CZTS. The adsorption of CZTS was affected by the addition of water. It was important to note that during the degradation of RhB by the CZTS/g-C_3N_4 composite structure, the maximum absorption peak of the solution had a blue shift to a large extent, mainly due to the gradual deethylation of RhB[50]. The maximum absorption peak in Fig.6(c) and Fig.6(d) decreased from 554 nm to 498 nm, respectively. RhB in the photocatalytic process would gradually deethylate to form intermediate products, and the absorption peak would continue to blue shift, and 498 nm was the final deethylation product of RhB corresponding absorption peak. It indicated that when RhB was degraded by CZTS/g-C_3N_4 composite structures, it was not degraded directly, but deethylated, and the process of deethylation and degradation at this composite ratio was slower. Fig.6(e) clearly showed the deethylation process of RhB, and the deethylation and degradation process were slower at this composite ratio. As shown in Fig.6(d), in the process of illumination for 10 min, RhB was rapidly deethylated and was degraded by CZTS/g-C_3N_4 composite structures and almost completely degraded within 60 min. The photocatalytic degradation curve showed that the CZTS/g-C_3N_4 composite structure had a good degradation effect on RhB and its intermediates.

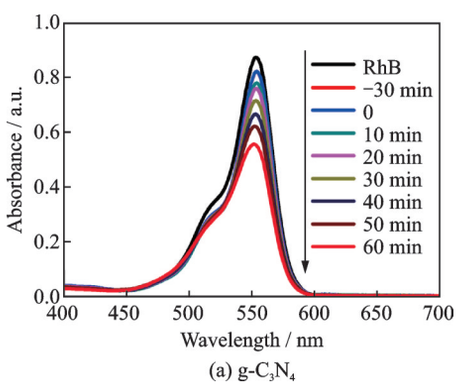

(a) g-C_3N_4

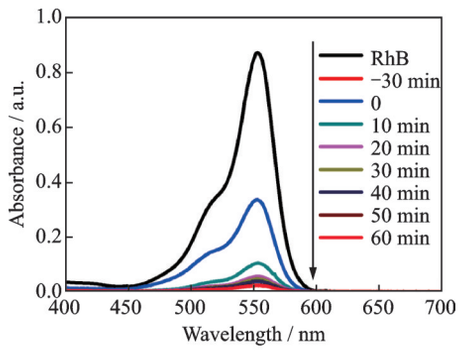

(b) CZTS

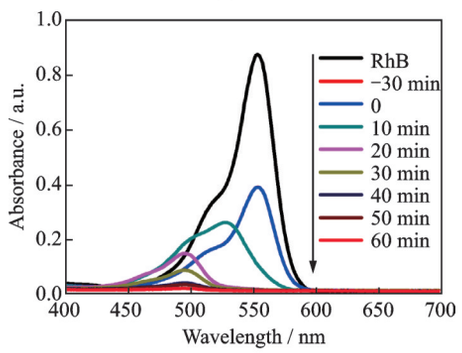

(c) CZTS/g-C_3N_4-1

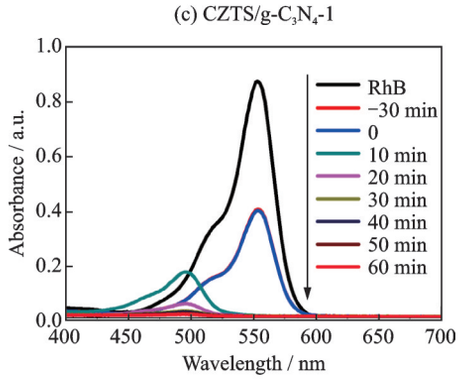

(d) CZTS/g-C_3N_4-2

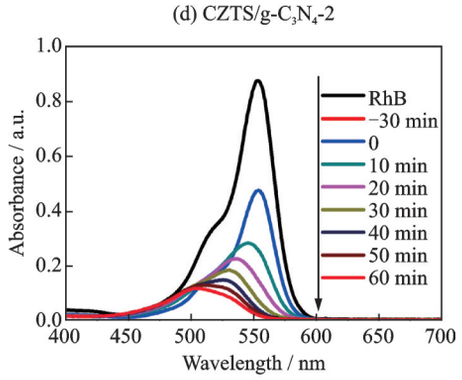

(e) CZTS/g-C_3N_4-3

Fig.6 Time-dependent UV-Vis absorption spectra of RhB solution under stimulated Vis irradiation

Fig.7(a) was the degradation efficiency curve of RhB under different catalyst conditions. The RhB solution without any photocatalyst had almost no change in its concentration regardless of whether it was during the dark treatment or the light period. The solution added with photocatalyst reached the

adsorption-desorption equilibrium after dark treatment for 30 min. After 60 min of illumination, the degradation rates of RhB in g-C_3N_4, CZTS, CZTS/g-C_3N_4-1, CZTS/g-C_3N_4-2 and CZTS/g-C_3N_4-3 samples were 36.67%, 97.28%, 98.00%, 98.63% and 87.00%, respectively. In our previous work, CZTS degraded 98.2% of RhB in 90 min, and the degradation rate was very slow in the last 30 min. Only 0.2% of RhB was degraded, almost reaching the degradation saturation. CZTS/g-C_3N_4 could degrade 98.63% of RhB in 60 min, which could further degrade RhB. Fig.7(b) shows the photocatalytic kinetic curves of RhB with different CZTS/g-C_3N_4 composite structure samples within a certain period. It could be seen that the curves were consistent with the apparent kinetic equation of the first order. After fitting, the degradation rate of RhB in the CZTS/g-C_3N_4-2 was 0.057 75 min^{-1}, while the degradation rates of g-C_3N_4 and CZTS were 0.006 3 and 0.040 41 min^{-1}, respectively. After calculation, the degradation rates of CZTS/g-C_3N_4-2 were 9.17 and 1.43 times that of g-C_3N_4 and CZTS, respectively. The degradation rate of RhB could be accelerated after the combination of g-C_3N_4 and CZTS. The cyclic degradation experiments of the CZTS/g-C_3N_4-2 were performed to characterize the cyclic stability of CZTS/g-C_3N_4-2. The results are shown in Fig.7(c). After five cycles, the degradation efficiency of RhB by CZTS/g-C_3N_4-2 was reduced by 11.87%, and the photocatalytic activity decreased, probably due to the incomplete cleaning of RhB and its intermediate products during the cleaning process. However, in general, after five photocatalytic degradation cycles, the samples remained in good photocatalytic activity. The XRD patterns before and after the photocatalytic degradation of RhB by CZTS/g-C_3N_4-2 were shown in Fig.7(d). After five photocatalytic degradation cycles, it was found that the position of the diffraction peak of the sample did not change except that the peak intensity decreased, indicating that the phase structure of CZTS/g-C_3N_4-2 did not change.

The general mechanism of photocatalysis is that the photocatalyst absorbs light energy to produce photogenerated carriers, which directly participates in the redox process of photocatalysis, or then generates $\cdot O^{2-}$, $\cdot OH$ radicals with solution[51]. In order to explore the key role of active substances in the photocatalytic process of the CZTS/g-C_3N_4,

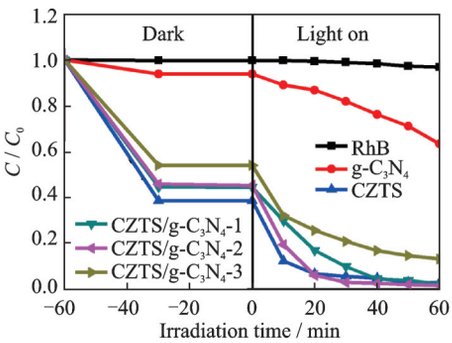

(a) Photocatalytic degradation variation of RhB concentration with the irradiation time under different catalyst conditions

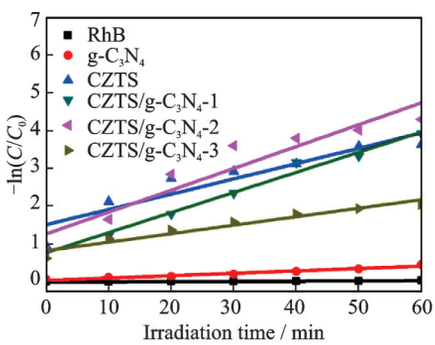

(b) Kinetic curves of RhB photocatalysis with different photocatalysts under visible light irradiation

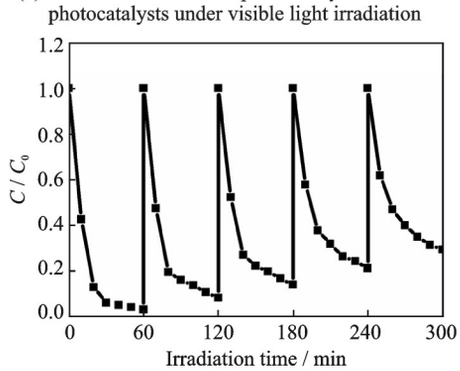

(c) Cyclic degradation curve of RhB by CZTS/g-C_3N_4-2

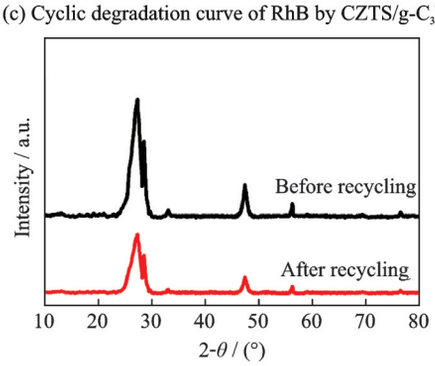

(d) XRD patterns of CZTS/g-C_3N_4-2 before and after five cycles

Fig.7 Photocatalytic performance diagram of CZTS/g-C_3N_4 composite and XRD patterns of CZTS/g-C_3N_4-2 before and after five cycles

photocatalytic activity capture experiments were carried out, and the possible mechanism of CZTS/g-C_3N_4 photocatalytic degradation of RhB was proposed. Ethylenediaminetetraacetic acid disodium (EDTA-2Na), $AgNO_3$, benzoquinone (BQ), and isopropanol (IPA) were used to capture h^+, e^-, $\cdot O^{2-}$ and $\cdot OH$ in the solution, respectively. Fig.8 shows the corresponding degradation effects of CZTS/g-C_3N_4-2 on RhB after adding different capture agents. The final degradation rate indicated that O^{2-} and e^- played a major role in the photocatalytic degradation of RhB with the composite structure of CZTS/g-C_3N_4-2. $\cdot OH$ played a weak role in CZTS/g-C_3N_4-2 photocatalytic degradation of RhB. When $\cdot O^{2-}$ and e^- were captured, the degradation rate of RhB was significantly reduced and there was no blue shift in the maximum absorption peak, whereas $\cdot O^{2-}$ was produced by the reaction of e^- with O_2 in the solution. The decrease of degradation rate after e^- capture since $\cdot O^{2-}$ could not be generated after e^- capture and the photocatalytic reaction could not continue. After h^+ capture, the degradation rate decreased, mainly because part of h^+ was directly involved in the degradation process. After capturing $\cdot OH$, the degradation rate was almost not proceeded, indicating that $\cdot OH$ played a weak role.

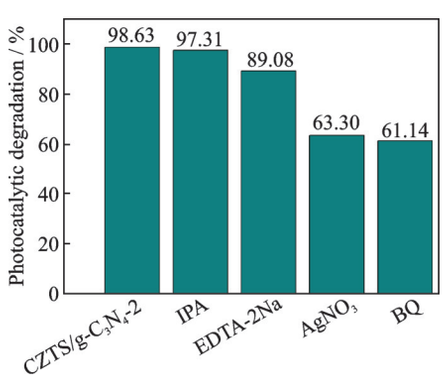

Fig.8 Radical trapping experiment of CZTS/g-C_3N_4-2

Therefore, based on the above experimental results, a possible mechanism of the photocatalytic effect of CZTS/g-C_3N_4 on RhB was proposed, and the photocatalytic mechanism was shown in Fig.9. In combination with DRS analysis, the LUMO of g-C_3N_4 was −1.21 eV and its the HOMO was and

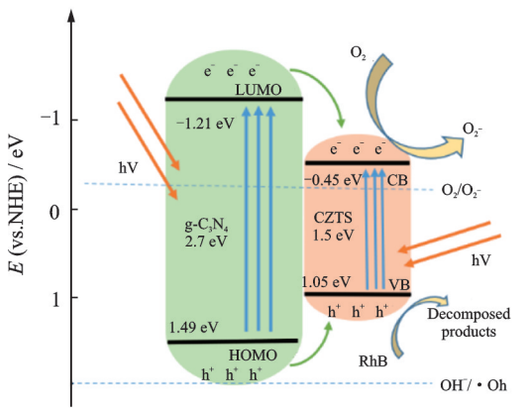

Fig.9 Mechanism of photocatalytic degradation of RhB by type-Ⅰ heterojunction of CZTS/g-C_3N_4

1.49 eV. The conduction band and valence band of CZTS nanomaterials were −0.45 eV and 1.05 eV, respectively. The type-Ⅰ heterojunction was therefore formed after the combination of CZTS and g-C_3N_4. The photogenerated carriers of g-C_3N_4 would migrate to CZTS under visible light. CZTS could be regarded as an electron capture hydrazine, and the electrons transferred from g-C_3N_4 to CZTS were captured by CZTS, which prolonged the lifetime of photogenerated electrons, thereby improving the photocatalytic reaction performance. Similar work has been reported in the previous piezocatalysts including CuS/KTN[52] and Bi_2S_3/KTN[53]. Through the synergistic effect of the CZTS/g-C_3N_4 heterostructure, the photogenerated carriers of g-C_3N_4 could be effectively separated. Although the final photogenerated carriers were concentrated on the band structure of CZTS, the yield of photogenerated carriers on CZTS increased significantly due to the charge transfer between the interfaces. When photocatalytic degradation of RhB, the photogenerated electrons were concentrated on the conduction band of CZTS, and reacted with dissolved oxygen in the solution to generate $\cdot O^{2-}$, which was a strong oxidizing substance in the subsequent deethylation and photocatalytic process. Meanwhile, the photogenerated holes were concentrated on the valence band of CZTS and directly degraded RhB. Under this mechanism, the photocatalytic performance of CZTS/g-C_3N_4 was significantly better than that of CZTS and g-C_3N_4.

3 Conclusions

The CZTS/g-C_3N_4 composite structure was successfully synthesized using a simple hydrothermal method. SEM images showed that flower-like CZTS and flake g-C_3N_4 were successfully combined. CZTS/g-C_3N_4 composite structure photocatalytically degraded RhB under visible light. After 60 min of illumination, the degradation efficiency of RhB by CZTS/g-C_3N_4 composite structure could reach 98.63%, and the degradation rates were 9.17 and 1.43 times that of g-C_3N_4 and CZTS, respectively. After five degradation cycles, the photocatalytic degradation efficiency of the CZTS/g-C_3N_4 composite structure decreased by 11.87%. By carrying out free radical capture experiments on CZTS/g-C_3N_4-2, the mechanism of photocatalytic degradation of CZTS/g-C_3N_4 composite structure was proposed. The main role played by CZTS/g-C_3N_4 in the photocatalytic degradation of RhB was that e^- reacted with dissolved oxygen in the solution to generate $\cdot O^{2-}$, followed by h^+. The composite structure of CZTS/g-C_3N_4 was type-Ⅰ heterojunction. Under visible light, the photogenerated carriers of g-C_3N_4 would migrate to the conduction band and valence band of CZTS. Through the synergistic effect of heterogeneous structures, the number of photogenerated carriers on CZTS was increased, thereby improving the photocatalytic effect.

References

[1] MEHRJOUEI M, MÜLLER S, MÖLLER D. A review on photocatalytic ozonation used for the treatment of water and wastewater[J]. Chemical Engineering Journal, 2015, 263: 209-219.

[2] PREETHI V, KANMANI S. Photocatalytic hydrogen production[J]. Materials Science in Semiconductor Processing, 2013, 16(3): 561-575.

[3] MO J, ZHANG Y, XU Q, et al. Photocatalytic purification of volatile organic compounds in indoor air: A literature review[J]. Atmospheric Environment, 2009, 43(14): 2229-2246.

[4] WANG H, ZHANG X, XIE Y. Recent progress in ultrathin two-dimensional semiconductors for photocatalysis[J]. Materials Science and Engineering: R: Reports, 2018, 130: 1-39.

[5] DAUB N A, AZIZ F, AZIZ M, et al. A mini review on parameters affecting the semiconducting oxide photocatalytic microbial disinfection[J]. Water, Air, & Soil Pollution, 2020, 231(9): 461.

[6] KANNAN K, RADHIKA D, SADASIVUNI K K, et al. Nanostructured metal oxides and its hybrids for photocatalytic and biomedical applications[J]. Advances in Colloid and Interface Science, 2020, 281: 102178.

[7] KUMAR J, BANSAL A. A comparative study of immobilization techniques for photocatalytic degradation of rhodamine b using nanoparticles of titanium dioxide[J]. Water, Air, & Soil Pollution, 2013, 224(3): 1452.

[8] SHENG J, TONG H, XU H, et al. Preparation and photocatalytic activity of SnO_2@TiO_2 core-shell composites modified by Ag[J]. Catalysis Surveys From Asia, 2016, 20(3): 167-172.

[9] OSIN O A, YU T, CAI X, et al. Photocatalytic degradation of 4-nitrophenol by C, N-TiO_2: Degradation efficiency vs. embryonic toxicity of the resulting compounds[J]. Frontiers in Chemistry, 2018, 6: 00192.

[10] PARZINGER E, MILLER B, BLASCHKE B, et al. Photocatalytic stability of single- and few-layer MoS_2[J]. ACS Nano, 2015, 9(11): 11302-11309.

[11] JIA T, MIN Z, CAO J, et al. Hydrothermal synthesis and visible-light photocatalytic activities of SnS_2 nanoflakes[J]. Journal of Wuhan University of Technology: Materials Science Edtion, 2015, 30(2): 276-281.

[12] CHENG J, HAN L, WEI Y, et al. Enhancement of photocatalytic property on ZnS/MoS_2 composite under visible light irradiation[J]. MATEC Web of Conferences, 2017, 108: 1008.

[13] PAWAR S M, PAWAR B S, MOHOLKAR A V, et al. Single step electrosynthesis of Cu_2ZnSnS_4 (CZTS) thin films for solar cell application[J]. Electrochimica Acta, 2010, 55(12): 4057-4061.

[14] KATAGIRI H. Cu_2ZnSnS_4 thin film solar cells[J]. Thin Solid Films, 2005, 480/481: 426-432.

[15] ITO K, NAKAZAWA T. Electrical and optical properties of stannite-type quaternary semiconductor thin films[J]. Japanese Journal of Applied Physics, 1988, 27(11): 2094-2097.

[16] KHERAJ V, PATEL K K, PATEL S J, et al. Synthesis and characterisation of copper zinc tin sulphide (CZTS) compound for absorber material in solar-cells[J]. Journal of Crystal Growth, 2013, 362: 174-177.

[17] WANG J, YU N, ZHANG Y, et al. Synthesis and performance of Cu_2ZnSnS_4 semiconductor as photocathode for solar water splitting[J]. Journal of Alloys and Compounds, 2016, 688: 923-932.

[18] KUSH P, DEORI K, KUMAR A, et al. Efficient hydrogen/oxygen evolution and photocatalytic dye degradation and reduction of aqueous Cr(vi) by surfactant free hydrophilic Cu_2ZnSnS_4 nanoparticles[J]. Journal of Materials Chemistry A, 2015, 3(15): 8098-8106.

[19] KRISHNAN A, KANNAN P. A non-van der waals two dimensional material from microwave synthesized Cu_2ZnSnS_4 nanocrystal agglomerates[J]. Materials Research Express, 2019, 6(11): 1150.

[20] ZOU Z, GAO Y, LONG F, et al. One-pot solvothermal synthesis of wurtzite Cu_2ZnSnS_4 nanocrystals[J]. Materials Letters, 2015, 158: 13-16.

[21] CHANG Z X, ZHOU W H, KOU D X, et al. Phase-dependent photocatalytic H_2 evolution of copper zinc tin sulfide under visible light[J]. Chemical Communications (Camb), 2014, 50(84): 12726-12729.

[22] FU X, JI Z, LI C, et al. Electrochemical method for synthesis of Cu_2ZnSnS_4 nanorod/TiO_2 nanotube arrays hybrid structure with enhanced photoelectrochemical properties[J]. Journal of Alloys and Compounds, 2016, 688: 1013-1018.

[23] COVEI M, BOGATU C, PERNIU D, et al. Comparative study on the photodegradation efficiency of organic pollutants using n-p multi-junction thin films[J]. Catalysis Today, 2019, 328: 57-64.

[24] ZUBAIR M, RAZZAQ A, GRIMES C A, et al. Cu_2ZnSnS_4 (CZTS)-ZnO: A noble metal-free hybrid Z-scheme photocatalyst for enhanced solar-spectrum photocatalytic conversion of CO_2 to CH_4[J]. Journal of CO_2 Utilization, 2017, 20: 301-311.

[25] RAZA A, SHEN H, HAIDRY A A, et al. Studies of Z-scheme WO_3-TiO_2/Cu_2ZnSnS_4 ternary nanocomposite with enhanced CO_2 photoreduction under visible light irradiation[J]. Journal of CO_2 Utilization, 2020, 37: 260-271.

[26] SRIDHARAN M, KAMARAJ P, HUH Y S, et al. Quaternary CZTS nanoparticle decorated CeO_2 as a noble metal free p-n heterojunction photocatalyst for efficient hydrogen evolution[J]. Catalysis Science & Technology, 2019, 9(14): 3686-3696.

[27] GUO L, ZHANG K, HAN X, et al. 2D/2D type-Ⅱ Cu_2ZnSnS_4/Bi_2WO_6 heterojunctions to promote visible-light-driven photo-Fenton catalytic activity[J]. Chinese Journal of Catalysis, 2020, 41(3): 503-513.

[28] WANG X, LI Y, ZHANG X, et al. Fabrication of a magnetically separable Cu_2ZnSnS_4/$ZnFe_2O_4$ p-n heterostructured nano-photocatalyst for synergistic enhancement of photocatalytic activity combining with photo-fenton reaction[J]. Applied Surface Science, 2019, 479: 86-95.

[29] CHONG R, WANG X, CHANG Z, et al. SiO_2 loading combined with high temperature calcination of kesterite Cu_2ZnSnS_4 nanocrystals towards enhanced photocatalytic H_2 evolution[J]. International Journal of Hydrogen Energy, 2017, 42(32): 20703-20710.

[30] YUAN M, WANG J, ZHOU W, et al. Cu_2ZnSnS_4-CdS heterostructured nanocrystals for enhanced photocatalytic hydrogen production[J]. Catalysis Science & Technology, 2017, 7(18): 3980-3984.

[31] KUMAR S, SURENDAR T, KUMAR B, et al. Synthesis of highly efficient and recyclable visible-light responsive mesoporous g-C_3N_4 photocatalyst via facile template-free sonochemical route[J]. RSC Advances, 2014, 4(16): 8132.

[32] FANG W, LIU J, YU L, et al. Novel (Na, O) co-doped g-C_3N_4 with simultaneously enhanced absorption and narrowed bandgap for highly efficient hydrogen evolution[J]. Applied Catalysis B: Environmental, 2017, 209: 631-636.

[33] ZHANG D, LIU T, AN C, et al. Preparation of vanadium-substituted polyoxometalate doped carbon nitride hybrid materials POM/g-C_3N_4 and their photocatalytic oxidation performance[J]. Materials Letters, 2020, 262: 126954.

[34] CHEN P, CHEN L, GE S, et al. Microwave heating preparation of phosphorus doped g-C_3N_4 and its enhanced performance for photocatalytic H_2 evolution in the help of Ag_3PO_4 nanoparticles[J]. International Journal of Hydrogen Energy, 2020, 45(28): 14354-14367.

[35] ZHANG Q, CHEN P, CHEN L, et al. Facile fabrica-

tion of novel Ag_2S/K-g-C_3N_4 composite and its enhanced performance in photocatalytic H_2 evolution[J]. Journal of Colloid and Interface Science, 2020, 568: 117-129.

[36] CHEN P, XING P, CHEN Z, et al. In-situ synthesis of $AgNbO_3$/g-C_3N_4 photocatalyst via microwave heating method for efficiently photocatalytic H_2 generation[J]. Journal of Colloid and Interface Science, 2019, 534: 163-171.

[37] CHEN Z, CHEN P, XING P, et al. Rapid fabrication of $KTa_{0.75}Nb_{0.25}$/g-C_3N_4 composite via microwave heating for efficient photocatalytic H_2 evolution[J]. Fuel, 2019, 241: 1-11.

[38] MKHALID I A, MOHAMED R M, ALHADDAD M, et al. Green synthesis of porous Cu_2ZnSnS_4/g-C_3N_4 heterostructured for promoted photocatalytic degradation of trichloroethylene[J]. Ceramics International, 2022, 48(8): 11736-11746.

[39] WU J, SHENG P, XU W, et al. Constructing interfacial contact for enhanced photocatalytic activity through $BiOIO_3$/g-C_3N_4 nano flake heterostructure[J]. Catalysis Communications, 2018, 109: 55-59.

[40] CAO Y, WU W, WANG S, et al. Monolayer g-C_3N_4 fluorescent sensor for sensitive and selective colorimetric detection of silver ion from aqueous samples[J]. Journal of Fluorescence, 2016, 26(2): 739-744.

[41] LI Z, JIANG G, ZHANG Z, et al. Phosphorus-doped g-C_3N_4 nanosheets coated with square flake-like TiO_2: Synthesis, characterization and photocatalytic performance in visible light[J]. Journal of Molecular Catalysis A: Chemical, 2016, 425: 340-348.

[42] LI J, LEI N, HAO H, et al. A series of BCN nanosheets with enhanced photoelectrochemical performances[J]. Chemical Physics Letters, 2017, 672: 99-104.

[43] SONG C, KIM S. Preparation and electrochemical characterization of Pt-supported flake-like graphitic carbon nitride on reduced graphene oxide as fuel cell catalysts[J]. Journal of the Electrochemical Society, 2015, 162(10): F1181-F1190.

[44] REN Q, WANG W, SHI H, et al. Synthesis and shape-dependent visible-light-driven photocatalytic activities of Cu_2ZnSnS_4 nanostructures[J]. Micro & Nano Letters, 2014, 9(8): 505-508.

[45] ALIREZAZADEH F, SHEIBANI S. Facile mechano-chemical synthesis and enhanced photocatalytic performance of Cu_2ZnSnS_4 nanopowder[J]. Ceramics International, 2020, 46(17): 26715-26723.

[46] RAZA A, SHEN H, HAIDRY A A. Novel Cu_2ZnSnS_4/Pt/g-C_3N_4 heterojunction photocatalyst with straddling band configuration for enhanced solar to fuel conversion[J]. Applied Catalysis B: Environmental, 2020, 277: 119239.

[47] BU Y, CHEN Z, XIE T, et al. Fabrication of C_3N_4 ultrathin flakes by mechanical grind method with enhanced photocatalysis and photoelectrochemical performance[J]. RSC Advances, 2016, 6(53): 47813-47819.

[48] ZHANG C, ZHANG H, ZHANG K, et al. Photocatalytic activity of $ZnWO_4$: Band structure, morphology and surface modification[J]. ACS Applied Materials & Interfaces, 2014, 6(16): 14423-14432.

[49] YANG Y, ZHANG W, XU Y, et al. Preparation of PbS and CdS cosensitized graphene/TiO_2 nanosheets for photoelectrochemical protection of 304 stainless steels[J]. Applied Surface Science, 2018, 452: 58-66.

[50] WEI Q, XU P, REN X, et al. Flower-like Cu_2ZnSnS_4 architectures synthetize and their visible-light catalytic properties[J]. Journal of Alloys and Compounds, 2019, 770: 424-432.

[51] RAZA A, SHEN H, HAIDRY A A, et al. In-situ synthesis of mesoporous TiO_2-Cu_2ZnSnS_4 heterostructured nanocomposite for enhanced photocatalytic degradation[J]. Applied Surface Science, 2020, 505: 144540.

[52] DAI X, CHEN L, LI Z, et al. CuS/$KTa_{0.75}Nb_{0.25}O_3$ nanocomposite utilizing solar and mechanical energy for catalytic N_2 fixation[J]. Journal of Colloid and Interface Science, 2021, 603: 220-232.

[53] CHEN L, DAI, X, LI X, et al. A novel Bi_2S_3/$KTa_{0.75}Nb_{0.25}O_3$ nanocomposite with high efficiency for photocatalytic and piezocatalytic N_2 fixation[J]. Journal of Materials Chemistry A, 2021, 9: 13344-1335.

Author Dr. **LI Yufang** received her Ph.D. degree in Institute of Metal Research from Chinese Academy of Sciences (CAS) in 2004. She is an associated professor in College of Materials Science and Technology of Nanjing University of Aeronautics and Astronautics (NUAA). Her current research interests include triboelectric nanogenerator, optoelectronic materials and solar cells.

Author contributions Dr. **LI Yufang** designed the study

and analyzed the data. Ms. **HOU Zhangchen** provided the data studies, explained the results and wrote the manuscript. Dr. **LIU Jinsong**, Mr. **SHI Zheng**, and Prof. **SHEN Honglie** contributed to the mechanism and discussion of the study. All authors commented on the manuscript draft and approved the submission.

Competing interests The authors declare no competing interests.

(Production Editor: ZHANG Bei)

CZTS/g-C_3N_4 Ⅰ型异质结中可见光驱动催化活性的提高

李玉芳[1], 侯张晨, 刘劲松, 施 政, 沈鸿烈

(南京航空航天大学材料科学与技术学院, 江苏省能源转换材料与技术重点实验室, 南京 211106, 中国)

摘要: 为了提高Cu_2ZnSnS_4(CZTS)光催化降解罗丹明B(RhB)的速率,本文采用水热法成功制备了CZTS/g-C_3N_4复合结构的Ⅰ型异质结并首次将CZTS/g-C_3N_4应用于光催化降解有色染料RhB。结果表明,g-C_3N_4附着在花状CZTS表面,两者形成Ⅰ型异质结。CZTS作为g-C_3N_4的电子陷阱,提高了载流子的分离效率。光催化降解RhB的结果表明,CZTS/g-C_3N_4复合结构可以提高RhB的光催化降解效果。RhB的最佳光催化效率在60 min内达到98.63%。

关键词: 光催化;热流体;CZTS/g-C_3N_4;光生载流子;异质结